

Dissipative descent: rocking and rolling down an incline

N. J. BALMFORTH¹, J. W. M. BUSH², D. VENER²
AND W. R. YOUNG³

¹Departments of Mathematics and Earth & Ocean Science, UBC, Vancouver BC, V6K 1Z2, Canada

²Department of Mathematics, MIT, Cambridge, MA 02139, USA

³Scripps Institution of Oceanography, UCSD, La Jolla, CA 92093-0213, USA

(Received 20 September 2006 and in revised form 23 June 2007)

We consider the dynamics of a hollow cylindrical shell that is filled with viscous fluid and another, nested solid cylinder, and allowed to roll down an inclined plane. A mathematical model is compared to simple experiments. Two types of behaviour are observed experimentally: on steeper slopes, the device accelerates; on shallower inclines, the cylinders rock and roll unsteadily downhill, with a speed that is constant on average. The theory also predicts runaway and unsteady rolling motions. For the rolling solutions, however, the inner cylinder cannot be suspended in the fluid by the motion of the outer cylinder, and instead falls inexorably toward the outer cylinder. Whilst ‘contact’ only occurs after an infinite time, the system slows progressively as the gap between the cylinders narrows, owing to heightened viscous dissipation. Such a deceleration is not observed in the experiments, suggesting that some mechanism limits the approach to contact. Coating the surface of the inner cylinder with sandpaper of different grades changes the rolling speed, consistent with the notion that surface roughness is responsible for limiting the acceleration.

1. Introduction

The ‘snailball’ is a magic trick wherein an apparently solid metal sphere rolls surprisingly slowly and erratically down an inclined plane. The explanation is that the sphere is not actually solid throughout, but a shell containing a second, smaller sphere and lubricated by a viscous fluid.† The acceleration of the device is arrested by viscous dissipation as the inner sphere falls through the fluid. The explanation fails to indicate why the rocking and rolling should be so erratic, and the details remain obscure.

As we demonstrate in this article, the same kind of rocking and rolling dynamics is observed when an analogous combination of cylinders rolls down an incline. The cylindrical arrangement factors out one spatial dimension from the dynamics (although two-dimensional motion is conceivably possible for the snailball, it

† The magic trick is marketed with the explanation: “A small, metallic gold ball just over 2 cm in diameter . . . this ball does roll, but it does so incredibly slowly. To an audience, it seems baffling why it should roll down a slope apparently in slow motion. You can pick the ball up, and it seems heavy, possibly solid. No clues if you shake it. However inside the ball, which is actually hollow, there is a viscous liquid and a smaller ball which is very heavy. When the Snail Ball rolls slowly down an incline, it is the smaller, heavier ball inside that determines the pace, and this is slow because of the viscous liquid.”

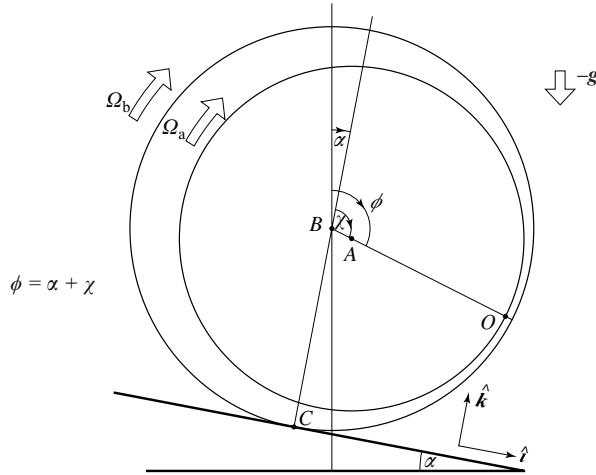


FIGURE 1. Point B is the centre of the outer cylinder (radius b) and A is the centre of the inner cylinder (radius a). In the (X, Z) -plane of the figure, clockwise rotations are positive. The displacement vector from B to A is $\epsilon(t)$. The ‘line of centres’ is BAO .

invariably rocks from side-to-side as it progresses downslope), and is more straightforward to deal with from the theoretical side. Thus, in this article, we present a combined theoretical and experimental study of the ‘snail cylinder’. Our purpose is to demystify the explanation of the dynamics and provide a mechanical foundation. We encounter some interesting facets to the problem that bear on the more general problem of the approach of rough solids through a viscous fluid.

The snail cylinder shares much in common with the journal bearing which has numerous applications in engineering (e.g. Pinkus & Sternlicht 1961). Unlike our present configuration, the outer shell of the journal bearing is fixed in place and forced to rotate at a prescribed rate. Moreover, although the axis of the inner cylinder is free to move, its rotation is also fixed. A configuration midway between the journal bearing and snail cylinder is an arrangement set up by Seddon & Mullin (2006) and Vener (2006), which fixes the outer cylinder but allows the inner cylinder to move and rotate freely.

The dynamics of the journal bearing, and indeed lubrication bearings of all geometries, is often explored using the Reynolds lubrication theory. We follow suit here and provide a lubrication theory of the snail cylinder. The lubrication approximation applies when the fluid inertia plays no role and when the fluid fills a relatively narrow gap. The generalization to Stokes flow in a snail cylinder without a thin gap, and more, can be found in Vener (2006).

2. Mathematical model

The geometry of our model is illustrated in figure 1. A hollow cylinder, with centre B and radius b , contains a smaller solid cylinder, with centre A and radius a ; we use the notation, $b = a + \delta$. The cylinders are not concentric, and their centres are displaced from one another by a distance $\epsilon(t)$ in a direction that can be specified by the angle $\chi(t)$, shown in figure 1, which lies between the line of centres and the perpendicular to the inclined plane. The angular speeds of the inner and outer cylinders are denoted by $\Omega_a(t)$ and $\Omega_b(t)$, respectively.

In the gap between the two cylinders there is a viscous fluid with density ρ and kinematic viscosity ν . The inner and outer cylinders have masses, m_a and m_b , respectively, whereas the fluid has mass $m_f = \pi(b^2 - a^2)L\rho$, with L denoting the axial length of the arrangement. In total, the apparatus has mass $M \equiv m_a + m_b + m_f$. The reduced mass of the inner cylinder is $m'_a \equiv m_a - m''_a$, where $m''_a \equiv \pi a^2 L \rho$ is the displaced mass of fluid.

The mathematical formulation of the model consists of equations of motion for the positions and rotations of the cylinders, plus the Navier–Stokes equations for the fluid; Appendix A summarizes the full formulation of the problem. We do not attack this complete formulation, but introduce the Stokes approximation to simplify the fluid part of the dynamics. However, because the arrangement as a whole is in motion down the incline, some subtlety is required because one can impose the approximation in different frames of reference (for example, one can use the inertial laboratory frame, or frames based on the centres of each cylinder). The overall fluid accelerations vary from frame to frame, and so the accuracy of the Stokes approximation probably hinges on which frame to select. We opt for the following: by introducing the Stokes approximation in the frame of reference of the centre of mass of the fluid, the acceleration of the fluid as a whole is incorporated into the dynamics and the residual accelerations about this mean may plausibly have their smallest effect. The details of this choice, and the ramifications for the dynamics are described in Appendix A; below we summarize the main equations of the motion that result, and then make the small-gap approximation of lubrication theory to give a compact description of the fluid forces and torques that enter those equations. This approximation, namely $b - a = \delta \ll a$, also allows us to simplify the equations of motion of the cylinders to arrive at a reduced model that we use to explore the dynamics.

2.1. The equations of motion

The configuration of the apparatus is specified by four independent variables, $\epsilon(t)$, $\chi(t)$, $\Omega_a(t)$ and $\Omega_b(t)$. The considerations of Appendix A indicate that the position of the inner cylinder is determined by the equations of motion,

$$\left(m_a + \frac{m''_a}{m_f}\right) (\epsilon \ddot{\chi} + 2\dot{\epsilon} \dot{\chi}) = f_\chi + m'_a g \sin \phi - m'_a b \dot{\Omega}_b \cos \chi, \quad (2.1)$$

$$\left(m_a + \frac{m''_a}{m_f}\right) (\ddot{\epsilon} - \epsilon \dot{\chi}^2) = f_\epsilon - m'_a g \cos \phi - m'_a b \dot{\Omega}_b \sin \chi, \quad (2.2)$$

where f_χ and f_ϵ represent the fluid forces in the direction of the line of centres and perpendicular to that direction, respectively. The combination, $m_a + m''_a/m_f$, is the effective inertial mass of the inner cylinder. The second terms on the right of (2.1) and (2.2) denote the Archimedean buoyancy force, and the final terms are d'Alembert forces arising because the position of the centre of the outer cylinder, to which the coordinates ϵ and χ are referred, does not lie in an inertial frame. The rotation of the inner cylinder follows from

$$\frac{1}{2} m_a a^2 \dot{\Omega}_a = T_a, \quad (2.3)$$

where T_a is the fluid torque.

Assuming that the outer cylinder rolls without sliding down the inclined plane, the equation of motion of the outer cylinder can be similarly broken down. Importantly, those equations contain the forces at the contact point with the plane, which one

can eliminate from the problem algebraically given that the rotation rate, Ω_b , also dictates the distance rolled. This leaves a single equation for $\Omega_b(t)$, as described in Appendix A. Alternatively, an equivalent equation follows from the total angular momentum balance,

$$\frac{d}{dt} \left[\frac{1}{2} m_a a^2 \Omega_a + (M + m_b) b^2 \Omega_b + \left(m_a + \frac{m_a''^2}{m_f} \right) \epsilon^2 \dot{\chi} + m_a' b \frac{d}{dt} (\epsilon \sin \chi) \right] + m_a' b \dot{\Omega}_b \epsilon \cos \chi \approx M g b \sin \alpha + m_a' g \epsilon \sin \phi, \quad (2.4)$$

where $\phi = \alpha + \chi$. Though (2.1)–(2.3) are exact, (2.4) contains our first approximation by neglecting the intrinsic angular momentum of the fluid in the frame of its centre of mass.

As the Stokes approximation describes the flow in the annular gap, the fluid remains in a state of instantaneous force balance. The forces, f_ϵ and f_χ , and torque, T_a , can then be computed as functions of the instantaneous geometrical arrangement (i.e. ϵ and χ) and velocities of the cylinder surfaces (given by Ω_a , Ω_b , $\dot{\epsilon}$ and $\dot{\chi}$). We do this via lubrication theory, as outlined in Appendix B, because our snail cylinders have relatively narrow gaps, although more general results exist (Finn & Cox 2001).

2.2. Lubrication approximation and a reduced model

In lubrication approximation, the fluid forces and torques, f_χ , f_ϵ and T_a , take the form (see Appendix B)

$$f_\epsilon = -\frac{12v a m_a''}{\delta^2} \frac{\dot{\kappa}}{(1 - \kappa^2)^{3/2}}, \quad (2.5)$$

$$f_\chi = \frac{12v a m_a'' \kappa (\Omega_a + \Omega_b - 2\dot{\chi})}{\delta^2 (2 + \kappa^2) \sqrt{1 - \kappa^2}}, \quad (2.6)$$

$$T_a = \frac{12v a m_a'' (1 - \kappa^2) (\Omega_b - \dot{\chi}) - (1 + 2\kappa^2) (\Omega_a - \dot{\chi})}{\delta 3(2 + \kappa^2) \sqrt{1 - \kappa^2}}, \quad (2.7)$$

where

$$\kappa(t) \equiv \frac{\epsilon(t)}{\delta}. \quad (2.8)$$

The equations of motion in (2.1), (2.2), (2.3) and (2.4), and the hydrodynamic quantities defined in (2.5)–(2.7), comprise a sixth-order dynamical system. However, some further simplifications are afforded by virtue of $\delta \ll a$. Moreover, unless the slope is small, the cylinder accelerates downhill. Hence, we focus on the distinguished limit in which also $\sin \alpha \sim \delta/a$. In this limit, the equations are systematically simplified by first non-dimensionalizing using the time scale

$$\tau \equiv 12 \frac{m_a'' v a}{m_a' \delta^2 g}. \quad (2.9)$$

We next introduce non-dimensional variables

$$(\hat{\Omega}_a, \hat{\Omega}_b) \equiv \tau (\Omega_a, \Omega_b), \quad (2.10)$$

and a non-dimensional time $\hat{t} \equiv t/\tau$. It is also convenient to work with $\phi = \chi + \alpha$.

Then, on suppressing the hats and to leading order in δ/a ,

$$\frac{\dot{\kappa}}{(1 - \kappa^2)^{3/2}} = -\cos \phi, \tag{2.11a}$$

$$\frac{\kappa(\Omega_a + \Omega_b - 2\dot{\phi})}{(2 + \kappa^2)(1 - \kappa^2)^{1/2}} = -\sin \phi, \tag{2.11b}$$

$$\frac{1}{2}\mathcal{Y}\dot{\Omega}_a = \frac{(1 - \kappa^2)(\Omega_b - \dot{\phi}) - (1 + 2\kappa^2)(\Omega_a - \dot{\phi})}{3(2 + \kappa^2)\sqrt{1 - \kappa^2}}, \tag{2.11c}$$

$$\mu\mathcal{Y}\dot{\Omega}_b + \frac{1}{2}\mathcal{Y}\dot{\Omega}_a = s + \kappa \sin \phi. \tag{2.11d}$$

In (2.11), the dimensionless combinations,

$$\mu \equiv \frac{M + m_b}{m_a}, \quad \mathcal{Y} \equiv \frac{g\delta^3}{144\nu^2} \frac{m_a m'_a}{m_a''^2}, \quad s \equiv \frac{a \sin \alpha}{\delta} \frac{M}{m'_a}, \tag{2.12}$$

are taken $O(1)$ (according to the values listed in the tables of §4, \mathcal{Y} lies in the range 10^{-2} to 5, whereas s ranges from 0.1 to 1).

3. Dynamics without cylinder contact

3.1. A steadily rolling equilibrium

The system (2.11) admits a simple equilibrium solution in which the apparatus rolls down the inclined plane at constant speed:

$$\left. \begin{aligned} 0 &= (1 - \kappa^2)\Omega_b - (1 + 2\kappa^2)\Omega_a, \\ 0 &= \cos \phi, \\ 0 &= \sin \phi + \frac{\kappa(\Omega_a + \Omega_b)}{(2 + \kappa^2)(1 - \kappa^2)^{1/2}}, \\ 0 &= s + \kappa \sin \phi. \end{aligned} \right\} \tag{3.1}$$

Thus,

$$\kappa = s, \quad \phi = -\frac{\pi}{2}, \quad \Omega_a = \frac{1 - s^2}{1 + 2s^2}\Omega_b, \quad \Omega_b = s^{-1}\sqrt{1 - s^2}(1 + 2s^2). \tag{3.2}$$

The result, $\phi = -\pi/2$, is a necessary consequence of the fact that when the motion is steady, the hydrodynamic forces are perpendicular to the line of centres and, therefore, can only balance gravity when that line is horizontal. More curiously, as the slope α decreases, so must the separation of the cylinder centres in the solution ($\epsilon = \delta\kappa \rightarrow \delta \sin \alpha$), with the result that the rolling speed increases (Ω_b in (3.2) is a monotonically decreasing function of s). The physical origin of this behaviour is that as $\alpha \rightarrow 0$, $\kappa \rightarrow 0$, and the cylinders become concentric, whereupon viscous dissipation cannot halt the descent of the device.

The equilibrium in (3.2) is the counterpart of the classical Sommerfeld solution in the lubrication theory of the journal bearing (Pinkus & Sternlicht 1961). Its curious properties are not physical because this solution is unrealizable: a linearization of (2.11) about this fixed point, plus a little algebra and judicious use of the Descartes rule of signs, establishes that this solution is linearly unstable (see Vener 2006). In other words, the model has no steady, stable rolling solution.

3.2. Sedimenting and sedimented solutions

Another special solution to the system can be found when $s = \Omega_a(0) = \Omega_b(0) = 0$, $\phi(0) = \pi$ and $\kappa(0) = \kappa_0$, and corresponds to placing the snail cylinder on a horizontal

plane, and then allowing the inner cylinder to fall vertically from a position directly underneath the centre of the outer cylinder, without either rotating. The solution has $\Omega_a(t) = \Omega_b(t) = 0$ and $\phi(t) = \pi$ for all t , and

$$\kappa(t) = \frac{t + \kappa_0/\sqrt{1 - \kappa_0^2}}{\sqrt{1 + (t + \kappa_0/\sqrt{1 - \kappa_0^2})^2}}. \quad (3.3)$$

As $t \rightarrow \infty$, we observe that $\kappa \rightarrow 1$. In other words, the inner cylinder ‘sediments’ onto the bottom surface of the outer cylinder, although contact takes an infinite time to occur. This result is equivalent to some well-known lubrication solutions for sedimentation (Goldman, Cox & Brenner 1967).

The ‘sedimented’ solutions, with $\kappa = 1$, form another analytically accessible class of solutions. With contact, we discard the first three relations of (2.11) and adopt

$$\kappa = 1, \quad \Omega_a = \Omega_b = \dot{\phi}. \quad (3.4)$$

The angular momentum balance (2.11) then reduces to

$$\Upsilon(\mu + \frac{1}{2})\ddot{\phi} - \sin \phi = s, \quad (3.5)$$

which is equivalent to the equation of motion of a ‘pushed pendulum’. In this solution the gap is closed and the fluid behaves like a solid, with the apparatus acting as an eccentrically weighted solid cylinder on an inclined plane. The orbits of the pushed pendulum can be classified into two types: for $s < 1$ and low initial speeds, the pendulum executes periodic oscillations, corresponding to the cylinders rocking back and forth about the fixed point, $\phi = -\sin^{-1} s$; for $s > 1$ or sufficiently large initial speed, on the other hand, the pendulum follows an unbounded winding solution that corresponds to acceleration downhill. Only the latter solutions give sustained progress down the inclined plane.

The stability of the rocking pushed pendulum solutions can be explored in system (2.11). To do this, we set $\zeta = \sqrt{1 - \kappa^2} \ll 1$. It then follows that

$$\dot{\zeta} = \zeta^2 \cos \phi + O(\zeta^3), \quad (3.6)$$

and

$$\Upsilon(\mu + \frac{1}{2})\ddot{\phi} - s - \sin \phi = 3\Upsilon^2(\mu^2 + \frac{1}{4})\zeta \frac{d^3\phi}{dt^3} + O(\zeta^2), \quad (3.7)$$

which can be attacked using the method of multiple scales. Of chief interest is the fixed point, $\sin \phi = -s$ ($\cos \phi = -\sqrt{1 - s^2}$) and $\Omega_a = \Omega_b = 0$, whose stability is determined by linearizing (3.6) and (3.7):

$$\dot{\zeta} \approx -\zeta^2 \sqrt{1 - s^2}, \quad \Upsilon(\mu + \frac{1}{2}) \frac{d^2\check{\phi}}{dt^2} + \sqrt{1 - s^2}\check{\phi} \approx 3\Upsilon^2(\mu^2 + \frac{1}{4})\zeta \frac{d^3\check{\phi}}{dt^3}, \quad (3.8)$$

where $\check{\phi} = \phi - \sin^{-1} s$. The multiple-scale solution is

$$\zeta = \frac{\zeta(0)}{1 + t\zeta(0)\sqrt{1 - s^2}}, \quad \check{\phi} = \left[1 + t\zeta(0)\sqrt{1 - s^2}\right]^{-q} e^{i\omega t} + \text{c.c.}, \quad (3.9)$$

with

$$\omega^2 = \frac{\sqrt{1 - s^2}}{\Upsilon(\mu + \frac{1}{2})}, \quad q = \frac{3(1 + 4\mu^2)}{2(1 + 2\mu)^2}, \quad (3.10)$$

indicating that this special point is always stable. In fact, the residual viscous dissipation present for $\zeta > 0$, which is given by the right-hand side of (3.7), causes the

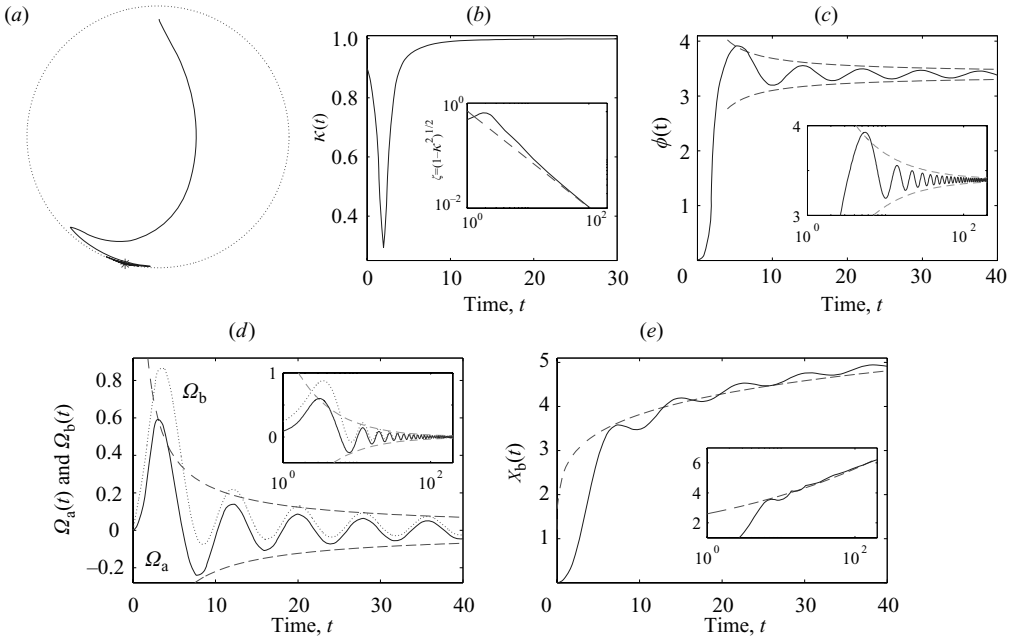


FIGURE 2. Sample rocking solution with $\Upsilon = 1$, $\mu = 1$ and $s = 1/4$: (a) the locus of the centre of the inner cylinder on the polar (κ, ϕ) plane (with $\phi = 0$ pointing vertically upwards), (b) $\kappa(t)$, (c) $\phi(t)$, (d) $\Omega_a(t)$ and $\Omega_b(t)$ and (e) $X_b(t)$. The initial position of the inner cylinder is shown, and $\Omega_a(0) = \Omega_b(0) = 0$. The star in (a) marks the limiting sedimentation solution; the dashed lines show the convergence to that solution expected from the multiple-scale solution of §3.2 (with some integration constants suitably chosen).

amplitude of all solutions with $|\zeta| \ll 1$ to decay secularly towards the fixed point. In other words, when the cylinders become close, they subsequently approach contact at $\phi = -\sin^{-1} s$.

Note that the exponent, q , varies from $5/6$ up to a maximum of $3/2$. Moreover, the decay to the fixed point, once one filters the fast oscillations of the pushed pendulum dynamics, is $\Omega_b \sim t^{-q}$, implying that $X_b \sim t^{1-q}$. Thus, there is a parameter range in which, even though the rotation rates are decreasing algebraically in time and the gap is closing, the device continues to roll down the plane.

3.3. Numerical results

To progress further, we solve the reduced model (2.11) numerically. Two types of solutions are obtained. First, when s is not too large, the inner cylinder settles vertically through the fluid; the outer cylinder rocks back and forth, and rolls slowly downhill; see figure 2. Ultimately the inner cylinder sediments onto the outer one, with a limiting solution, $\kappa \rightarrow 1$, $(\Omega_a, \Omega_b) \rightarrow (0, 0)$ and $\sin \phi \rightarrow -s$, as $t \rightarrow \infty$. The convergence to that solution follows the predictions of the multiple-scale theory outlined above. In particular, because $\mu = 1$ is chosen in the computation, the position of the device on the incline, X_b , increases like $t^{1/6}$.

Second, when s is too large (exceeding a value just below unity, and depending on initial conditions), the solution locks into a runaway rolling solution as illustrated in

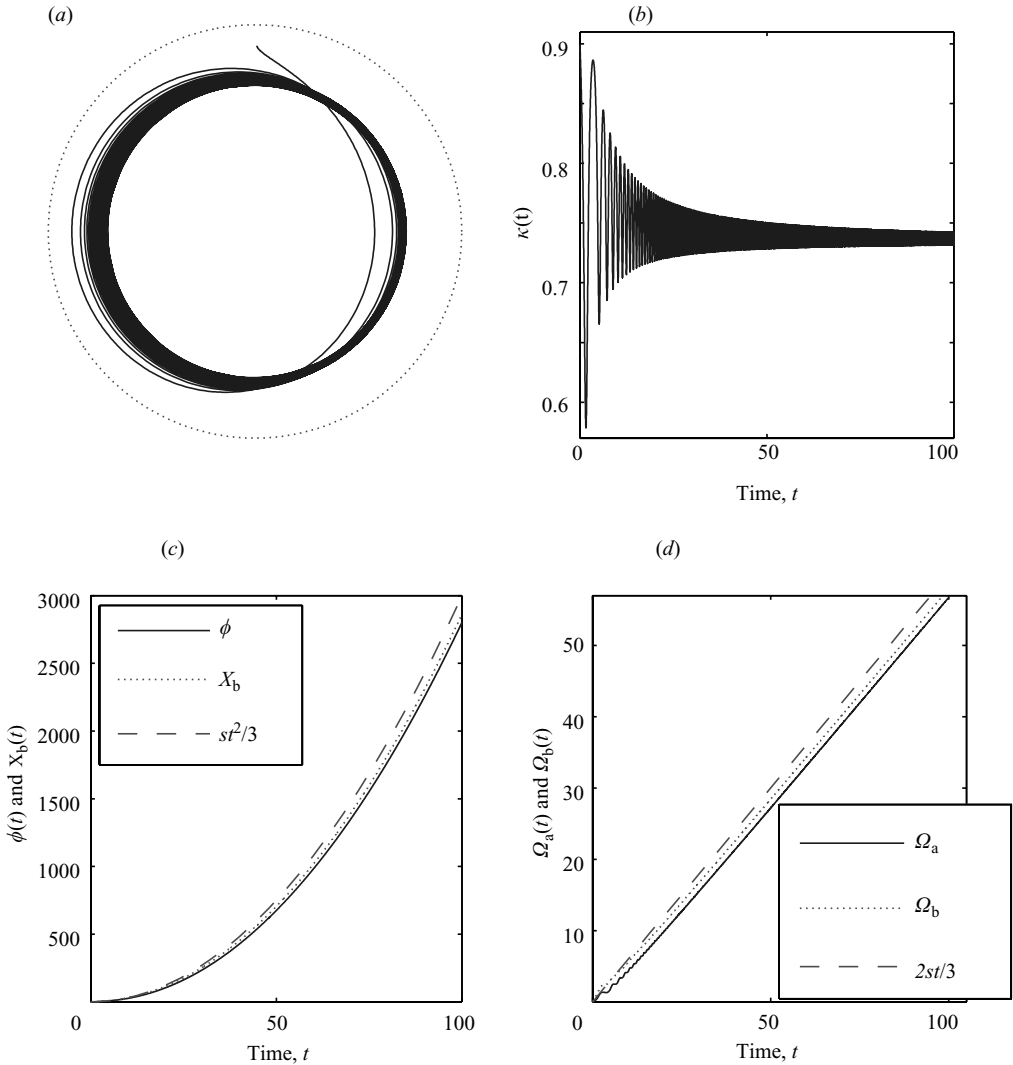


FIGURE 3. Sample rolling solution with $\gamma = \mu = 1$ and $s = 0.9$, showing (a) a polar plot of the inner cylinder position, (b) $\kappa(t)$, (c) $\phi(t)$ and $X_b(t)$, and (d) $\Omega_a(t)$ and $\Omega_b(t)$. The dashed lines show the expected limiting rolling solution (3.11).

figure 3. The runaway solution has the limiting form

$$\Omega_a \sim \Omega_b \sim \dot{\phi} \sim \frac{st}{(\mu + \frac{1}{2})\gamma}, \tag{3.11}$$

and corresponds to the dimensional rolling speed, $Mgt \sin \alpha / (M + m_b + \frac{1}{2}m_a)$.

Over a range of s , both rocking and rolling solutions are possible; which state emerges is selected by the initial condition. The sedimenting, rocking solution disappears for $s \geq 1$, and only rolling solutions are possible beyond that critical slope. The rolling solution can also persist at relatively small values of s , although

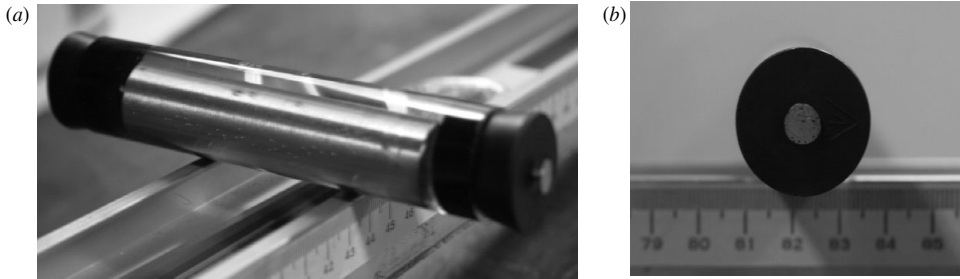


FIGURE 4. Photographs showing various views of the snail cylinder. The views are (a) angled from the front and (b) edge on. Note that several small bubbles are trapped inside and have risen to the top of the fluid, and that the inner cylinder lies close to its lowest point.

	Density	Radius	Mass	Length
Steel inner cylinder	7.85 g cm^{-3}	0.78 cm	158 g	10.35 cm
Aluminium inner cylinder	2.7 g cm^{-3}	0.78 cm	55 g	10.35 cm
Outer cylinder		1.125 cm	47 g	13.7 cm
Oil	$0.92 - 0.96 \text{ g cm}^{-3}$		24 g	

TABLE 1. Physical data. The viscosities of the different grades of silicone oil (Dow Corning 200 fluid) were approximately 5×10^{-5} , 2×10^{-4} , 3.5×10^{-4} and $5 \times 10^{-4} \text{ m}^2 \text{ s}^{-1}$; that of the canola oil was about $6 \times 10^{-5} \text{ m}^2 \text{ s}^{-1}$. The Perspex outer cylinder was 1.5 mm thick, and its inner radius is listed. The runway was inclined by various angles between 1° and 5.6° .

the initial conditions required to reach the runaway state become increasingly unlikely.

4. Experimental phenomenology

To compare with the theoretical predictions outlined above, we conducted a suite of experiments with a snail cylinder made of a Perspex tube containing silicone or canola oil and a steel or aluminium inner cylinder. A photograph of the apparatus is shown in figure 4. The ends of the tube were stoppered by black rubber corks, which were inserted as straight as possible. To assist with the filling of the device with oil, metal nails were inserted through the middle of each cork. During the experiments, the nails were pushed through to protrude slightly (less than a millimetre) into the fluid, and prevent the inner cylinder from moving too close to the corks. Whenever that cylinder became too close to the nails, the experiment was stopped. Each experiment was started after shaking the device a little so that the inner cylinder did not lie very close to the outer one. Physical data for the apparatus are given in table 1; this translates to the parameters listed in table 2.

As predicted by theory, depending on the inclination of the runway, two types of characteristic motion are observed: when the slope is relatively shallow, a slow, rocking and rolling motion ensues; on high slopes, the cylinder accelerates under gravity. The two characteristic motions are illustrated in figures 5 and 6, respectively, which show the distance travelled along the runway, X , as a function of time, t . In the second case, the runaway acceleration is largely independent of the viscosity of the fluid and closely follows the law $X = \frac{1}{3}gt^2 \sin \alpha$, which matches the theoretical model above since $2(M + m_b + \frac{1}{2}m_a)/M \approx 3$ for the aluminium cylinder.

a	δ	L	m_b	M	m_a	m'_a	m''_a	μ	q	
0.8 cm	0.325 cm	10.35 cm	47 g	Steel Alum.	229 g 127 g	158 g 55 g	134 g 34 g	21 g 21 g	1.75 3.11	0.98 1.14

TABLE 2. Physical parameters for the model. The fluid mainly fills the gap between the two curved surfaces of the cylinders (about 4 g of the total 24 g resides at the ends). Also listed are the parameters μ and q defined in (2.12) and (3.10).

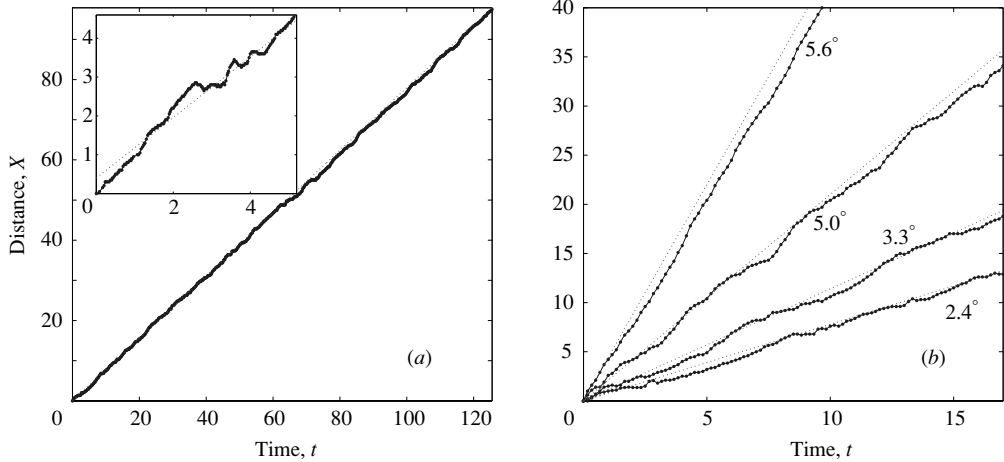


FIGURE 5. Distance travelled along the runway for a steel inner cylinder with various slopes. (a) A long run at 2.4° ; the inset shows a magnification of the path. (b) Four different slopes, as marked. The dotted lines show the best linear fits calculated for all the experiments. $\nu = 2 \times 10^{-4}$.

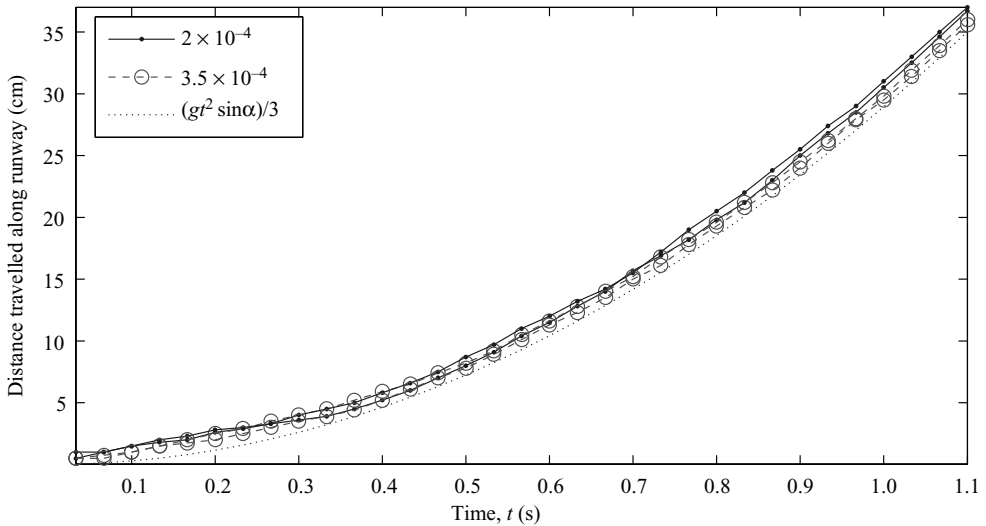


FIGURE 6. Distance travelled along the runway for an aluminium inner cylinder with a slope of 5° . Four experiments are shown: a first pair of repeated runs with $\nu = 2 \times 10^{-4}$ (dots and solid lines), and a second pair with $\nu = 3.5 \times 10^{-4}$ (circles and dashed lines). Also shown is the function $(gt^2 \sin \alpha)/3$ (dotted lines).

In contrast, the details of the low-slope rocking behaviour disagree with the theory: first, cylinders on shallow slopes roll erratically down the ramp, rocking back and forth as they progress. Second, the speed is roughly steady and described well by a linear fit over long times, as shown by the time series in figure 5. The inset in panel (a) shows a detailed short path, and displays the unsteady, rocking progression of the outer cylinder. Instead, theory predicts that the cylinders rock regularly whilst progressively decelerating, with the aluminium arrangement stopping after a finite distance ($q \approx 1.14 > 1$) and the steel one continuing to make (increasingly slow) progress ($q \approx 0.98 < 1$).

Observations through the Perspex wall of the outer cylinder show that the rocking corresponds to irregular, differential motion of the two cylinders. In particular, throughout the evolution the inner cylinder lies close to its lowest possible point, but is dragged slightly up the rear side of the outer cylinder. The rocking corresponds to irregular sliding and rolling of the inner cylinder over the lower surface of the outer one. Again, no such motion is predicted theoretically.

The key problem is that the model predicts that a slow rolling of the snail cylinder cannot suspend the inner cylinder inside the fluid; the gap must continually thin, leading to the deceleration of the device. In reality, the cylinders continue to make roughly steady progress, suggesting that the gap never closes. One possible explanation is offered by the roughness of the cylinder surfaces: asperities could, in principle, prevent full contact of the cylinders and maintain a minimum gap through which fluid continues to flow. The cylinders then become free to roll steadily at a rate given by the roughness of the surfaces. A similar argument was put forward by Smart, Beimfohr & Leighton (1993) for the motion of a sphere down an inclined plane.

5. Dynamics with a rough contact

When asperities on the surfaces of the two cylinders touch, a contact force must be included in the equations of motion. This contact force contains a normal reaction, \mathcal{C}_ϵ (directed along the line of centres), that holds the cylinders apart, and a tangential frictional component, \mathcal{C}_χ , that acts to equalize the two rotation speeds. The cylinders are thereby prevented from moving closer than a certain critical distance, $\kappa \leq \kappa_* < 1$, allowing fluid flow through the gap to generate finite viscous forces and torques; κ_* parameterizes the roughness scale.

As described more fully in Appendix C, the reduced model can be modified to include the leading-order effects of the contact forces. The main casualties are the radial equation of motion (2.11a) and the torque balance (2.11c), which become

$$-\cos \phi = \begin{cases} (1 - \kappa^2)^{-3/2} \dot{\kappa} & \text{if } \kappa < \kappa_* \\ \mathcal{C}_\epsilon & \text{if } \kappa = \kappa_*, \end{cases} \quad (5.1)$$

and

$$\frac{(1 - \kappa^2)(\Omega_b - \dot{\phi}) - (1 + 2\kappa^2)(\Omega_a - \dot{\phi})}{3(2 + \kappa^2)\sqrt{1 - \kappa^2}} = \begin{cases} \frac{1}{2} \gamma \dot{\Omega}_a & \text{if } \kappa < \kappa_* \\ \frac{1}{2} \gamma \dot{\Omega}_a + \mathcal{C}_\chi & \text{if } \kappa = \kappa_*, \end{cases} \quad (5.2)$$

respectively, where $(\mathcal{C}_\epsilon, \mathcal{C}_\chi)$ denotes the (suitably non-dimensionalized) contact force. The angular equation of motion (2.11b) remains unchanged because the frictional contact force first enters when it becomes comparable to the viscous torque, which is order δ/a smaller than the lubrication pressure force, f_χ . Moreover, total angular momentum balance (2.11d) is not affected by either of the contact forces.

Assuming the standard model of friction, the two components of the contact force are related by

$$|\mathcal{C}_x| \leq |\mathcal{C}_\epsilon| \tan \psi, \quad (5.3)$$

where ψ is a friction angle. There are two options contained in (5.3): either the normal force is sufficiently strong to lock the cylinder surfaces together, or the surfaces are held together more weakly and slide over one another with $|\mathcal{C}_x| = |\mathcal{C}_\epsilon| \tan \psi$. Given that $\Omega_a = \Omega_b$ when the cylinders are locked together (for a narrow gap with $a \approx b$), we find from (2.11*b*) and (5.2) that

$$\mathcal{C}_x = -\frac{2s + (1 - 2\mu)\kappa_* \sin \phi}{2(1 + 2\mu)}. \quad (5.4)$$

Thus, locking results when

$$\left| \frac{2s + (1 - 2\mu)\kappa_* \sin \phi}{2(1 + 2\mu)} \right| < |\cos \phi| \tan \psi. \quad (5.5)$$

To solve the modified system as an initial-value problem, we evolve the system from a state in which the inner cylinder is suspended in the fluid ($\kappa(0) < \kappa_*$) up to a ‘collision time’, $t = t_*$, at which the surfaces touch and $\kappa(t_*) = \kappa_*$. Beyond that instant, we set $\mathcal{C}_\epsilon = -\cos \phi$ to continue the solution, monitoring whether or not the traction between the cylinders is sufficient to overcome friction and force the surfaces to slide over one another. Should (5.5) be satisfied, we set $\Omega_a = \Omega_b$ and solve (2.11*b, d*) with (5.2) relegated to a diagnostic equation for \mathcal{C}_x (the system then reduces to the equation for a dissipative, pushed pendulum). If (5.5) is violated, on the other hand, the cylinders maintain a sliding contact; we solve (2.11*b, d*) and (5.2), with $\mathcal{C}_x = \cos \phi \tan \psi \operatorname{sgn}(\Omega_b - \Omega_a)$ (the choice of sign ensures that the friction drags the rotation rates together).

We illustrate the behaviour in figure 7. For the example shown, the ultimate state of the system is a steadily rolling solution in which the cylinders are in sliding contact. A case in which the final rolling solution has the cylinders locked together by friction is shown in figure 8. Note that the computation switches abruptly between the different versions of the model equations. In particular, when the cylinders first come into contact, if friction is sufficient to lock the cylinders together, then Ω_a must jump discontinuously at the moment of contact. This can be rationalized physically in terms of an instantaneous impulse that affects the inner cylinder. In principle, at collision, there should also be an equal and opposite impulse acting on the outer cylinder. However, that cylinder is also resting on its contact point with the inclined plane, and the model effectively assumes that any impulse from the collision of the two cylinders is taken up by the other contact.

The addition of a rough contact therefore allows the cylinder arrangement to approach a steady rolling solution. In reality, the minimum gap size, κ_* , is unlikely to be uniform over the surfaces of the cylinders, and more probably would be a complicated function of the orientations of both. A simple way to extend the model to incorporate such an effect is to add slight stochastic variations in κ_* . Solutions would then converge to irregularly rolling states in which the system is randomly kicked from equilibrium and then rocks slowly back, with obvious similarities to the observations. In principle, the unsteadiness offers insight into the variations of κ_* .

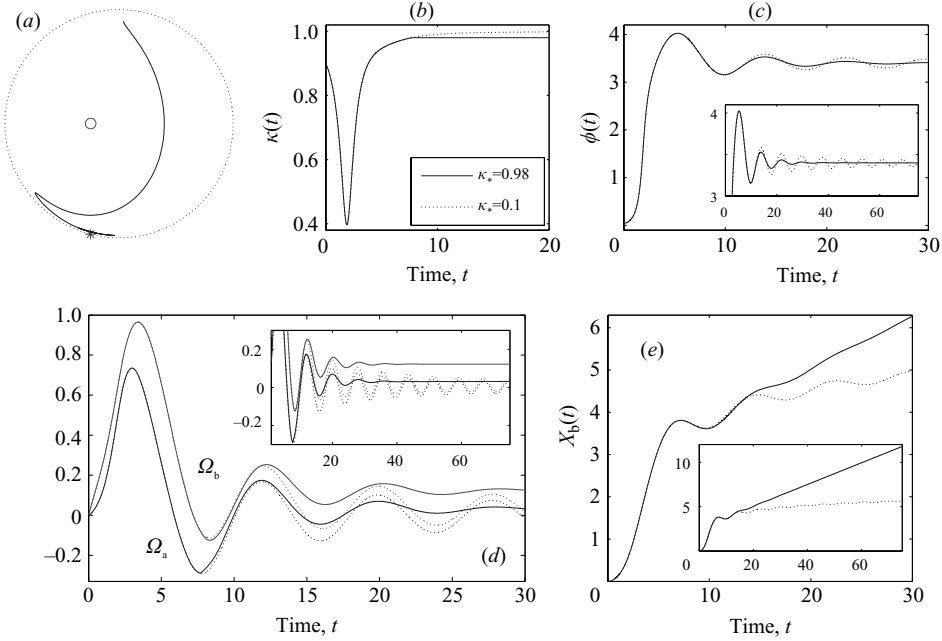


FIGURE 7. Sample rocking solution for $\Gamma = \mu = 1$ and $s = 1/4$, with κ limited to the range $(0, \kappa_* = 0.98)$, and $\psi = 0.05$. Panels (a–d) are as for figure 2, except that the unlimited sedimenting solution is also shown by the dotted lines.

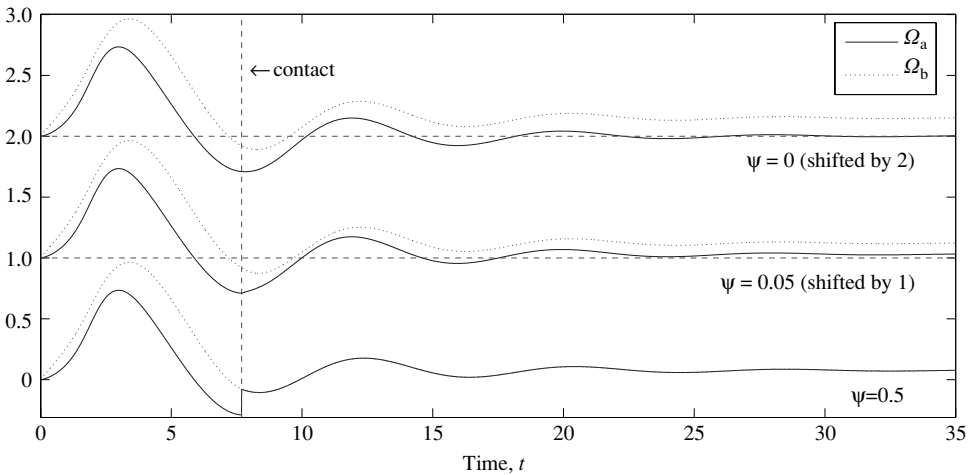


FIGURE 8. Sample solution for $\Gamma = \mu = 1$ and $s = 1/4$, with $\kappa_* = 0.98$ and three values of ψ (0.5, 0.05 and 0; the curves are offset of clarity). The vertical dashed line shows the moment of contact.

The fixed point to which the solution converges is given by

$$\kappa_* \sin \phi = -s, \tag{5.6}$$

$$\sin \phi = -\frac{\kappa_*(\Omega_a + \Omega_b)}{(2 + \kappa_*^2)(1 - \kappa_*^2)^{1/2}}, \tag{5.7}$$

$$\cos \phi = -\mathcal{C}_\epsilon, \tag{5.8}$$

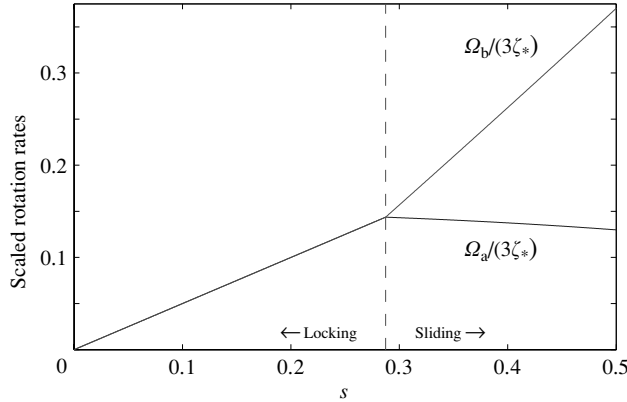


FIGURE 9. Scaled, steady rotation rates, $\Omega_a/(3\zeta_*)$ and $\Omega_b/(3\zeta_*)$, for $\psi = 0.15$ rad.

$$\frac{(1 - \kappa_*^2)\Omega_b - (1 + 2\kappa_*^2)\Omega_a}{3(2 + \kappa_*^2)\sqrt{1 - \kappa_*^2}} = \mathcal{C}_\chi. \tag{5.9}$$

The condition (5.5) for locking now reduces to $s < 2\sqrt{1 - s^2/\kappa_*^2} \tan \phi$, implying

$$\Omega_a = \Omega_b = \frac{1}{2\kappa_*^2} s(2 + \kappa_*^2)\sqrt{1 - \kappa_*^2}. \tag{5.10}$$

Otherwise,

$$\Omega_a = \frac{s(1 - \kappa_*^2)^{3/2}}{2\kappa_*^2} - 3\sqrt{1 - \kappa_*^2} \cos \phi \tan \psi, \quad \Omega_b = \frac{s(2 + \kappa_*^2)}{2\kappa_*^2} \sqrt{1 - \kappa_*^2} - \Omega_a. \tag{5.11}$$

When the minimum gap is relatively narrow, and $\zeta_* \equiv \sqrt{1 - \kappa_*^2} \ll 1$, we may write both solutions in the compact form,

$$\Omega_a = 3\zeta_* s \text{ Min} \left(\frac{1}{2}, \frac{\sqrt{1 - s^2}}{s} \tan \psi \right), \quad \Omega_b = 3\zeta_* s \text{ Max} \left(\frac{1}{2}, 1 - \frac{\sqrt{1 - s^2}}{s} \tan \psi \right). \tag{5.12}$$

The steady rolling speeds predicted by these formulae are illustrated in figure 9.

6. Comparison of theory and experiment

6.1. Outer cylinder speeds

In dimensional terms, the limiting cylinder speed with rough contact is expected to be

$$V = V_* \times \sin \alpha \times \zeta_* \text{ Max} \left(\frac{1}{2}, 1 - \frac{\sqrt{1 - s^2}}{s} \tan \psi \right). \tag{6.1}$$

Equation (6.1) divides the speed into three factors: a velocity scale,

$$V_* = \frac{bM\delta g}{4vm''_a}, \tag{6.2}$$

the main dependence on slope, $\sin \alpha$, and a final factor dependent on the surface properties. On the smaller slopes, (6.1) reduces to $V = (V_*\zeta_*/2) \sin \alpha$.

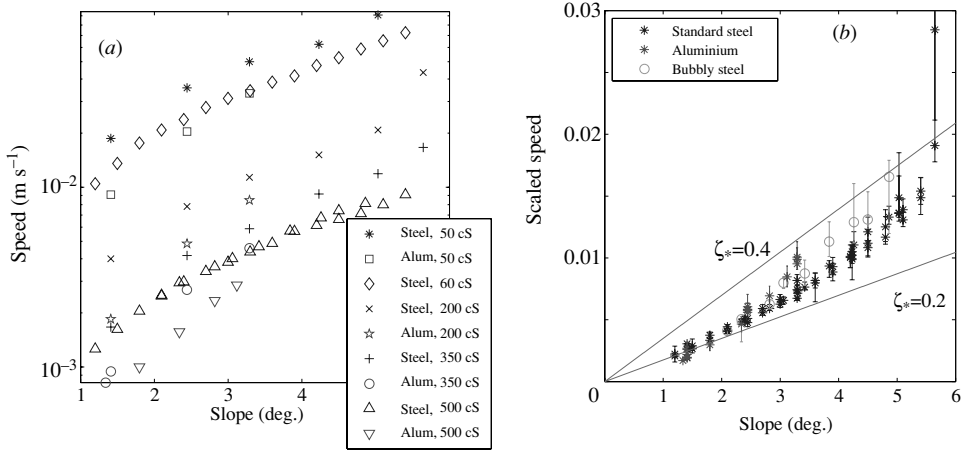


FIGURE 10. The average speeds fitted to the experiments. (a) The raw data, plotted against slope, with the different symbols corresponding to different viscosities, and inner cylinders. In (b) we scale the speeds by the factor V_* in (6.2), and add errorbars based on the variations between several experiments. The two lines show theoretical predictions assuming $V/V_* = (\zeta_*/2) \sin \alpha$ with $\zeta_* = 0.1$ and 0.2 . The data shown by circles indicate measurements taken for 500 cs oil in which a large number of small bubbles are entrained in the fluid and migrate into the narrowest part of the gap between the cylinders.

Average speeds of the outer cylinder in the experiments are shown in figure 10. These averages are obtained either by linear fits to the recorded position, or by taking the mean of the time required to roll 25 cm during several different experiments. As illustrated in figure 10(b), a scaling of the speeds by the velocity scale, V_* , compresses the data close to a single curve that depends slightly on the inner cylinder material.

Also drawn in figure 10 are the lines $V/V_* = (\zeta_*/2) \sin \alpha$, with $\zeta_* = 0.2$ and 0.4 . The comparison with the experimental data suggests that $\zeta_* \sim 0.2$. In turn, because

$$\zeta_* \equiv \sqrt{1 - \kappa_*^2} = \sqrt{1 - \left(1 - \frac{\sigma}{b-a}\right)^2}, \quad (6.3)$$

where σ is the minimum gap width, this implies a maximum roughness scale of $\sigma \sim 50$ microns. This estimate is consistent with images taken of the surface of the cylinders with a microscope which revealed roughness of that order.

To explore further the dependence of cylinder speed on surface roughness, we conducted more experiments in which the steel cylinder was first covered with differing grades of sandpaper (more specifically, we used 50, 80, 120, 150 and 220 ‘grit’, American CAMI standard). The roughened cylinder speeds are compared to those of the original, smooth cylinder in figure 11, and are faster by an amount depending on the grade of sandpaper, confirming the dependence on the scale of roughness. As shown in figure 11(b), the data can be collapsed further when we scale by a roughness factor, ζ_* , given by the values for σ listed in table 3 (speed data for the smooth cylinder also collapse onto that of the roughened cylinders if we adopt a roughness scale of 50 microns). In the inset of the picture, the estimated roughness scale, σ , is plotted against the mean particle size of the sandpaper, as given by the the American CAMI standard. The roughness scale is about four times the mean particle size in each of the five cases used. We conclude that rough contact provides a plausible rationalization of

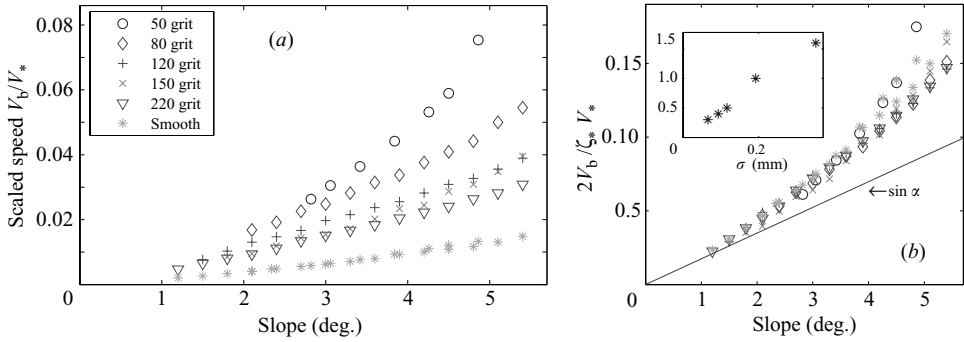


FIGURE 11. Cylinder speeds with sandpaper-coated inner cylinders. (a) Average speeds of the outer cylinder scaled by V_* against slope for the steel inner cylinder and 500 cS silicone oil. The stars indicate the speeds with the usual, smooth cylinder. In (b), a further scaling of $\zeta_*/2$ is used to collapse the data. The values of ζ_* are calculated using the roughness scales, σ , listed in table 3. The inset plots the inferred σ -values against the mean particle size of the sandpaper (according to the American CAMI standard).

Grade	220	150	120	80	50	Smooth
Inferred (mm)	0.3	0.4	0.5	1	1.6	0.05
Expected (mm)	0.07	0.09	0.12	0.2	0.36	

TABLE 3. Roughness scales for the various grades of sandpaper (as given by the ‘grit’ value listed). The ‘inferred’ value indicates the number used to collapse the data in figure 11; the ‘expected’ value is the number quoted by the American CAMI standard and refers to average particle size.

the experimental results, although the comparison cannot be used to test the theory without knowing further details of the sandpaper particle distribution.

Note that the data begin at increasingly large inclination angles as the roughness of the sandpaper increases. This is because the object could come to a halt on the runway if the slope was too small, which is consistent with the notion that when contact occurs between the cylinders, any roughness in the surfaces can allow inclined points of equilibrium.

It was also very difficult to avoid entraining small air bubbles into the silicone oil when filling the apparatus. In the lower viscosity fluids, the bubbles appeared to collect and merge into one or two bigger bubbles that rose to the top of the fluid and stayed there whilst the cylinders rolled down the runway (as is visible in figure 4). In these cases, we did not observe any smaller bubbles collecting in the low-pressure regions occurring near the line of closest approach of the cylinders. However, with the higher viscosity (500 cS) oil, the action of filling and even rapid rolling appeared to create many small bubbles that took several hours to coalesce. When the cylinders were rolled down the runway with such ‘bubbly’ oil, we noted a systematic increase of speed of up to 20 %, especially for higher slopes (see figure 10). In these cases, the small bubbles were clearly migrating into the narrowest part of the fluid-filled gap. Thus, the presence of bubbles can affect the rolling speed just as cavitation affects the dynamics of the journal bearing (see Pinkus & Sternlicht 1961) and spheres rotating adjacent to walls (see Prokunin 2004, Seddon & Mullin 2006 and Yang *et al.* 2006).

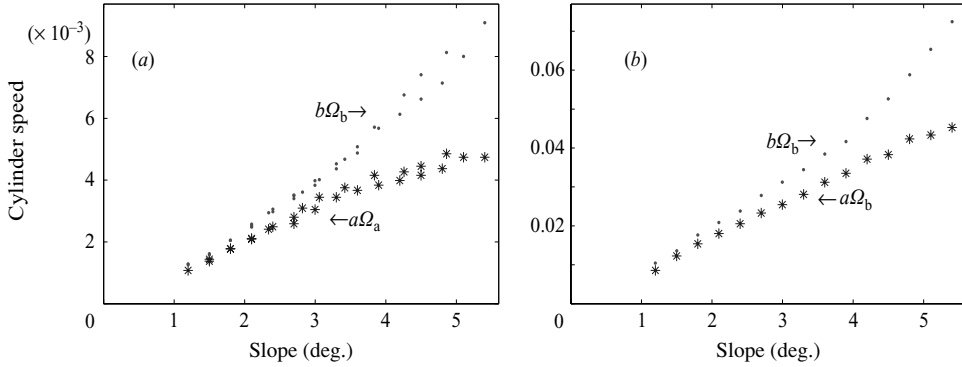


FIGURE 12. Average speeds of the two cylinders, $\langle V_a \rangle = a \langle \Omega_a \rangle$ (stars) and $\langle V_b \rangle = b \langle \Omega_b \rangle$ (dots), against slope for the steel inner cylinder and (a) 500 centiStoke and (b) 60 centiStoke oil.

6.2. Inner cylinder speeds

The observed rolling speeds in figures 10 and 11 noticeably steepen with increasing slope. The theoretical rationalization of this behaviour is that the cylinders are locked into the same rotation rate on shallow slopes due to the friction of contact. As the slope is increased, however, the cylinders begin sliding over one another, and the outer cylinder then rolls faster down the incline, whilst the inner one rotates less quickly.

To look for an analogous behaviour in the experiments, we measured the rotation of the inner cylinder by tracking surface markers. Figure 12 shows the results, plotting the average speeds, $\langle V_b \rangle = b \langle \Omega_b \rangle$ and $\langle V_a \rangle = a \langle \Omega_a \rangle$, against the runway slope (where the angular brackets signify averages over 1 m). As predicted, the cylinder speeds are closely matched on shallow slopes, and the two cylinders roll over one another like the cogs of a gear; on steeper slopes, the rotation speeds diverge from one another, with the inner cylinder rotating less rapidly.

Although the measurements in figure 12 agree qualitatively with theory, there are some differences in the details. Theory, for example, predicts that the cylinders should be perfectly locked for low slope, and that sliding should set in suddenly at a critical inclination given by

$$\tan \psi = \frac{s}{2\sqrt{1-s^2}}. \quad (6.4)$$

In contrast, the experimental data show no such abrupt change in behaviour, and the low-slope rotation speeds do not match perfectly. However, given that the minimum gap is not likely to be the same all the way around the cylinder surfaces, it is unlikely that the cylinders could ever become perfectly locked, and a more gradual transition would then result. The data suggest a transition on slopes of about 3° , which offers an estimate of the friction angle for the sliding of the cylindrical surfaces over one another in oil. One other notable point of disagreement is that, in the theory, the rotation rate of the inner cylinder decreases once sliding sets in; the observations show no such tendency.

7. Discussion

Our goal in this work has been to develop a theoretical model of the snail cylinder and compare it with experiments. Provided the model includes a mechanism that limits the closing of the gap between the two cylinders, it is possible to rationalize the

observed phenomenology of the device and quantitatively reproduce the dependence of the rolling speed and style on the various physical parameters. Here, we have focused on a rough contact between the cylinders as the required mechanism. However, inertia and cavitation provide two other possibilities.

Inertia breaks the symmetry of the Stokes pressure distribution and can levitate suspended objects. For the problem at hand, inertial lift is surely negligible for the slowest, most viscous configurations in which the inner cylinder sits almost at its lowest point and the gap is at its thinnest (the Reynolds number for flow of 500 cS oil through a gap of order tens of microns at speeds of mm s^{-1} is 10^{-4} or less). Even for the least viscous, fastest configurations, the Reynolds number barely surpasses unity when the gap is at its widest. Overall, the Stokes approximation appears to offer a reliable simplification of the dynamics.

Cavitation is conventionally thought to be important in the journal bearing (Pinkus & Sternlicht 1961), and has been demonstrated to be crucial in the dynamics of spheres rolling adjacent to walls (Prokunin 2004; Ashmore, del Pino & Mullin 2005; Yang *et al.* 2006). Indeed, our experiments indicate that the presence of bubbles does influence the rolling speed: in several runs with the more viscous oils, small bubbles accumulated near the narrowest part of the fluid gap. The rolling speed was then noticeably faster than in cases for which no such line of bubbles was discernible in the gap. However, the change in rolling speed was not extreme (amounting to less than about 20%), and bubbles did not migrate into the gap in the less viscous cases. Furthermore, simple modifications of the model that accounted for bubbles or cavitation by truncating the pressure distribution when it approached too low a value (a trick used for the journal bearing; see also Ashmore *et al.* 2005) were unable to provide sufficient lift to counter gravity (Vener 2006) and allow steady rolling. Although neither argument is conclusive, we feel that the most plausible explanation of constant speed rolling is rough contact.

Finally, we comment on the relevance of our results to the snailball magic trick. Although the phenomenology of the rolling dynamics of the two configurations is observed to be similar, sedimenting cylinders and spheres show important differences as contact is approached (Goldman *et al.* 1967; Jeffrey & Onishi 1981). It is conceivable that this may have ramifications for the rolling dynamics of the two configurations. We leave this issue open for future work.

This work was supported by the National Science Foundation under the Collaborations in Mathematical Geosciences initiative (grant numbers ATM0222109 and ATM0222104). J.B. gratefully acknowledges the support of a National Science Foundation Career Grant (CTS-0130465). We thank Keith Bradley of the Coastal Research Laboratory, Woods Hole Oceanographic Institution, for assistance in building the snail cylinder.

Appendix A. Derivation of the equations of motion

A.1. Geometry

The geometry is shown in figure 1. We use a Cartesian coordinate system attached to a plane which is inclined at an angle α to the horizontal; the unit vector \hat{i} points down the slope and the unit normal \hat{k} is perpendicular to the plane. The unit vector \hat{j} is into the page in figure 1, and clockwise rotations are positive. The position vector

is $\mathbf{X} = X\hat{\mathbf{i}} + Z\hat{\mathbf{k}}$ and the gravitational acceleration is $-\mathbf{g}$, where

$$\mathbf{g} = -g(\sin\alpha\hat{\mathbf{i}} - \cos\alpha\hat{\mathbf{k}}). \quad (\text{A } 1)$$

In this (X, Z) -coordinate system, the two cylinders have centres at the positions $\mathbf{X}_a = X_a\hat{\mathbf{i}} + Z_a\hat{\mathbf{k}}$ and $\mathbf{X}_b = X_b\hat{\mathbf{i}} + Z_b\hat{\mathbf{k}}$, respectively. The requirement that the outer cylinder rolls without slipping down the plane dictates that

$$\dot{X}_b = b\Omega_b, \quad Z_b = b. \quad (\text{A } 2)$$

Geometry implies that the centre of the inner cylinder is given by

$$\mathbf{X}_a = \mathbf{X}_b + \boldsymbol{\epsilon}, \quad \boldsymbol{\epsilon} \equiv \epsilon(\sin\chi\hat{\mathbf{i}} + \cos\chi\hat{\mathbf{k}}). \quad (\text{A } 3)$$

Thus the distance between the centres A and B is denoted by $\epsilon(t)$, and $\chi(t)$ is the angle between the line of centres and the Z -axis. We denote the angle between the line of centres and the direction of gravity by $\phi(t) \equiv \alpha + \chi(t)$.

The centre of mass of the fluid is

$$\mathbf{X}_f \equiv m_f^{-1} \int \rho \mathbf{X} \, dA_f, \quad (\text{A } 4)$$

where the integral is over $A_f(t)$, the moving domain of the fluid. Geometric considerations show that

$$m_f \mathbf{X}_f = m_f \mathbf{X}_b - m_a'' \boldsymbol{\epsilon}. \quad (\text{A } 5)$$

With the relations above, one finds that the centre of mass of the whole apparatus, $M\mathbf{X}_c = m_a\mathbf{X}_a + m_b\mathbf{X}_b + m_f\mathbf{X}_f$, is at

$$M\mathbf{X}_c = M\mathbf{X}_b + m_a' \boldsymbol{\epsilon}. \quad (\text{A } 6)$$

The relations above express \mathbf{X}_a , \mathbf{X}_f and \mathbf{X}_c in terms of our main independent variables \mathbf{X}_b and $\boldsymbol{\epsilon}$.

A.2. Motion of the cylinders

In our inertial, (X, Z) -frame, the equations of motion of the two cylinders are

$$m_a \ddot{\mathbf{X}}_a = \mathbf{F}_a - m_a \mathbf{g}, \quad (\text{A } 7)$$

$$m_b \ddot{\mathbf{X}}_b = \mathbf{F}_b - m_b \mathbf{g} + \mathbf{E}. \quad (\text{A } 8)$$

\mathbf{F}_a and \mathbf{F}_b denote the forces that the fluid exerts on the two cylinders; \mathbf{E} is the external force exerted on cylinder B at the point of contact (C in figure 1) with the plane. \mathbf{E} consists of the friction force E_X , acting along the plane, that prevents the outer cylinder from freely sliding downhill, and the normal reaction, E_Z , required to hold the cylinder on the plane: $\mathbf{E} = E_X\hat{\mathbf{i}} + E_Z\hat{\mathbf{k}}$.

The rotations of the two cylinders satisfy the angular equations of motion,

$$\frac{1}{2}m_a a^2 \dot{\Omega}_a = T_a, \quad (\text{A } 9)$$

$$m_b b^2 \dot{\Omega}_b = T_b - bE_X. \quad (\text{A } 10)$$

Here T_a and T_b denote the clockwise torques about the cylinder centres, A and B , exerted by the fluid. The term $-bE_X$ on the right of (A 10) is the torque about the centre B exerted by the force \mathbf{E} . Above we have assumed that the inner cylinder is a uniform solid so that the moment of inertia is $m_a a^2/2$, and that B is a cylindrical shell with moment of inertia $m_b b^2$.

A.3. Motion of the fluid

The fluid has velocity, $\mathbf{U}(X, Z, t)$, and pressure, $P(X, Z, t)$. The Navier–Stokes equations are

$$\rho(\mathbf{U}_t + \mathbf{U} \cdot \nabla \mathbf{U}) = -\nabla P + \rho\nu \nabla^2 \mathbf{U} - \rho \mathbf{g}, \quad \nabla \cdot \mathbf{U} = 0, \quad (\text{A } 11)$$

with $\nabla \equiv (\partial_X, \partial_Z)$.

The force per unit area exerted on the fluid at a boundary with outward normal $\hat{\mathbf{n}}$ is \mathfrak{F} , where

$$\mathfrak{F}_i \equiv -P n_i + \rho\nu(U_{i,j} + U_{j,i})n_j. \quad (\text{A } 12)$$

Integration of (A 11) over the domain $A_f(t)$ occupied by the fluid provides a differential equation for the centre of mass of the fluid:

$$m_f \ddot{\mathbf{X}}_f = -\mathbf{F}_a - \mathbf{F}_b - m_f \mathbf{g}. \quad (\text{A } 13)$$

In (A 7), (A 8) and (A 13) we calculate the forces as

$$\mathbf{F}_a \equiv -L \oint \mathfrak{F} d\ell_a, \quad (\text{A } 14)$$

where $d\ell_a$ is the line element at the surface of cylinder A , with a similar expression for \mathbf{F}_b .

To obtain the angular momentum balance for the fluid, we take the cross-product of (A 11) with \mathbf{X} and integrate:

$$\rho L \frac{d}{dt} \int \mathbf{X} \times \mathbf{U} dA_f = -(T_a + T_b) \hat{\mathbf{j}} - \mathbf{X}_a \times \mathbf{F}_a - \mathbf{X}_b \times \mathbf{F}_b - m_f \mathbf{X}_f \times \mathbf{g}, \quad (\text{A } 15)$$

where the torques

$$T_a \hat{\mathbf{j}} = -L \oint (\mathbf{X} - \mathbf{X}_a) \times \mathfrak{F} d\ell_a \quad \text{and} \quad T_b \hat{\mathbf{j}} = -L \oint (\mathbf{X} - \mathbf{X}_b) \times \mathfrak{F} d\ell_b, \quad (\text{A } 16)$$

are defined about the cylinder centres A and B , just as in (A 9) and (A 10).

Summing (A 7), (A 8) and (A 13) we obtain the total momentum equation of the apparatus,

$$M \ddot{\mathbf{X}}_c = \mathbf{E} - M \mathbf{g}. \quad (\text{A } 17)$$

The total angular momentum equation, obtained by combining (A 7), (A 8), (A 9), (A 10) and (A 15), is

$$\begin{aligned} \frac{d}{dt} \left(m_a \mathbf{X}_a \times \dot{\mathbf{X}}_a + m_b \mathbf{X}_b \times \dot{\mathbf{X}}_b + \frac{1}{2} m_a a^2 \Omega_a \hat{\mathbf{j}} + m_b b^2 \Omega_b \hat{\mathbf{j}} + \rho L \int \mathbf{X} \times \mathbf{U} dA_f \right) \\ = -M \mathbf{X}_c \times \mathbf{g} - X_b E_Z \hat{\mathbf{j}}. \end{aligned} \quad (\text{A } 18)$$

The right-hand side consists of the total gravitational torque, and the moment of the external force, \mathbf{E} , about the origin of the (X, Z) -coordinate system.

A.4. The frame of reference of the fluid

To complete the equations formulated above, we must calculate the fluid forces, \mathbf{F}_a and \mathbf{F}_b , and torques, T_a and T_b . To this end, we implement the Stokes approximation in the frame of reference in which the centre of mass of the fluid remains at rest. We move to that fluid frame with the transformation

$$\mathbf{x} \equiv \mathbf{X} - \mathbf{X}_f(t), \quad \mathbf{u}(\mathbf{x}, t) \equiv \mathbf{U}(\mathbf{X}, t) - \dot{\mathbf{X}}_f(t). \quad (\text{A } 19)$$

Introducing

$$p \equiv P + \rho(\mathbf{g} + \ddot{\mathbf{X}}_t) \cdot \mathbf{x}, \quad (\text{A } 20)$$

we recast the Navier–Stokes equations as

$$\rho(\mathbf{u}_t + \mathbf{u} \cdot \nabla \mathbf{u}) = -\nabla p + \rho\nu \nabla^2 \mathbf{u}, \quad (\text{A } 21)$$

where above $\nabla \equiv (\partial_x, \partial_z)$. By analogy with (A 12) we introduce

$$\mathfrak{f}_i \equiv -pn_i + \rho\nu(u_{i,j} + u_{j,i})n_j, \quad (\text{A } 22)$$

so that $\mathfrak{F} = \mathfrak{f} + [\rho(\mathbf{g} + \ddot{\mathbf{X}}_t) \cdot \mathbf{x}] \hat{\mathbf{n}}$.

In terms of p and \mathbf{u} the total hydrodynamic forces in (A 14) are

$$\mathbf{F}_a = \mathbf{f} + m_a''(\mathbf{g} + \ddot{\mathbf{X}}_t) \quad \text{and} \quad \mathbf{F}_b = -\mathbf{f} - (m_t + m_a'')(\mathbf{g} + \ddot{\mathbf{X}}_t), \quad (\text{A } 23)$$

where

$$\mathbf{f} \equiv -L \oint \mathfrak{f} d\ell_a. \quad (\text{A } 24)$$

A key intermediate identity used to obtain (A 23) and (A 24) from the expression for \mathbf{F}_a in (A 14) is

$$\oint x_i n_j d\ell = \int dA \delta_{ij}. \quad (\text{A } 25)$$

In (A 24) we have defined \mathbf{f} by integrating round the surface of cylinder A . Evaluating the integral at the surface of cylinder B gives $-\mathbf{f}$, which is a consequence of working in the frame defined by \mathbf{X}_t , so that $\int \mathbf{u} dA_t = 0$ at all times.

The torque, T_a , defined in (A 16), can be written in terms of p and \mathbf{u} as

$$T_a \hat{\mathbf{j}} = -L \oint (\mathbf{x} - \mathbf{x}_a) \times \mathfrak{f} d\ell_a, \quad (\text{A } 26)$$

where $\mathbf{x}_a = (1 + m_a''/m_t)\boldsymbol{\epsilon}$ is the position of the centre of cylinder A in the fluid frame. The torque, T_b , is provided by $\mathbf{a} \rightarrow \mathbf{b}$ in (A 26). An intermediate identity used to obtain (A 26) from the expression for T_a in (A 16) is

$$\varepsilon_{ijk} \oint x_j n_k x_m d\ell = \varepsilon_{ijm} \int x_j dA. \quad (\text{A } 27)$$

A.5. Motion of the inner centre relative to the outer centre: the $\boldsymbol{\epsilon}$ equation

We rewrite the equation of motion of the inner cylinder, (A 7), in terms of $\boldsymbol{\epsilon}$, \mathbf{f} and Ω_b , and use (A 23) to replace \mathbf{F}_a by \mathbf{f} . With (A 3) and (A 5) we then arrive at

$$\left(m_a + \frac{m_a''^2}{m_t} \right) \ddot{\boldsymbol{\epsilon}} = \mathbf{f} - m_a' \mathbf{g} - m_a' b \Omega_b \hat{\mathbf{i}}. \quad (\text{A } 28)$$

It is convenient to represent the hydrodynamic force as

$$\mathbf{f} = f_\epsilon \hat{\boldsymbol{\epsilon}} + f_\chi \hat{\boldsymbol{\chi}}. \quad (\text{A } 29)$$

f_ϵ and f_χ denote the components of the hydrodynamic force on the inner cylinder. The unit vector $\hat{\boldsymbol{\epsilon}} = \boldsymbol{\epsilon}/|\boldsymbol{\epsilon}|$ is directed from B to A (increasing ϵ); $\hat{\boldsymbol{\chi}} = \hat{\mathbf{j}} \times \hat{\boldsymbol{\epsilon}}$ is perpendicular to $\hat{\boldsymbol{\epsilon}}$ and orientated in the direction of increasing χ . If we now resolve the equation of motion of the inner cylinder (A 28) in terms of these polar variables centred on B , we obtain the two equations of motion (2.1)–(2.2) quoted in §2.

With (A 9), (2.1) and (2.2) we have three equations involving $[\chi, \epsilon, \Omega_a, \Omega_b]$. To obtain a fourth equation relating these variables we turn to the total angular

momentum equation (A 18). We make our first approximation by neglecting the intrinsic angular momentum of the fluid, $\int \mathbf{U} \times \mathbf{X} \, dA_t$, and we evaluate all the remaining angular momenta and torques in terms of $[\chi, \epsilon, \Omega_a, \Omega_b]$. This gives equation (2.4) of § 2.

Appendix B. Lubrication analysis

For lubrication theory, it is convenient to move into a coordinate system in which the centres of the cylinders are not moving, and position a polar coordinate system, (r, θ) , at the inner cylinder (i.e. on point *A* in figure 1). The angle θ is measured positive in the clockwise direction with $\theta = 0$ running along the line of centres, *BAO*, and passing through the narrowest point of the gap. Then the gap width $h(\theta)$ is approximately

$$h(\theta) = \delta - \epsilon \cos \theta, \tag{B 1}$$

where $\delta \equiv b - a \ll a$. We then use a ‘gap coordinate’, $0 \leq z \leq h(\theta)$, defined by $r \equiv a + z$ so that $(z, \theta) = (0, 0)$ is the point *O* in figure 1.

To leading order in δ/a , the lubrication equations take the form

$$\rho \nu u_{zz} = a^{-1} p_\theta, \quad p_z = 0, \quad \frac{1}{a} u_\theta + w_z = 0. \tag{B 2}$$

These must be solved subject to the velocity boundary conditions on the cylinders.

In our new frame of reference, the fluid flow is dictated by the motions of the two cylinders. Those motions can be divided into a rotational part generated by the two rotations, $\Omega_a - \dot{\phi}$ and $\Omega_b - \dot{\phi}$, and a ‘squeeze flow’ in which the cylinders move towards each other with a speed $\dot{\epsilon}$, squeezing out the fluid from the narrowest part of the gap. To ease the construction of the fluid forces and torques, we split the lubrication problem into these two parts and construct the full solution via linear superposition.

B.1. The rotational flow, $u^R(z, \theta)$

To leading order, the boundary conditions are

$$u^R(0, \theta) = a(\Omega_a - \dot{\phi}), \quad w^R(0, \theta) = 0, \tag{B 3}$$

$$u^R(h, \theta) = a(\Omega_b - \dot{\phi}), \quad w^R(h, \theta) = 0. \tag{B 4}$$

The solution is

$$u^R(z, \theta) = \left(1 - \frac{z}{h}\right) a(\Omega_a - \dot{\phi}) + \frac{z}{h} a(\Omega_b - \dot{\phi}) - \frac{p_\theta^R}{2a\rho\nu} z(h - z). \tag{B 5}$$

An integral of the continuity equation in z then provides the condition

$$q = \int_0^h u^R(z, \theta) \, dz = \frac{ah}{2} (\Omega_b + \Omega_a - 2\dot{\phi}) - \frac{h^3 p_\theta^R}{12a\rho\nu}. \tag{B 6}$$

Moreover, since $\oint p_\theta^R \, d\theta = 0$,

$$q = a\delta(\Omega_b + \Omega_a - 2\dot{\phi}) \frac{1 - \kappa^2}{2 + \kappa^2}, \tag{B 7}$$

with $\kappa \equiv \epsilon/\delta$. The result (B 7) is obtained using the integrals

$$\oint \frac{d\theta}{1 - \kappa \cos \theta} = \frac{2\pi}{\sqrt{1 - \kappa^2}}, \quad \oint \frac{d\theta}{(1 - \kappa \cos \theta)^2} = \frac{2\pi}{(1 - \kappa^2)^{3/2}} \tag{B 8}$$

$$\oint \frac{d\theta}{(1 - \kappa \cos \theta)^3} = \frac{\pi(2 + \kappa^2)}{(1 - \kappa^2)^{5/2}}. \quad (\text{B } 9)$$

Returning to (B6), and eliminating q with (B7), we obtain

$$p_\theta^{\text{R}}(\theta) = \frac{12a^2 \rho v}{h^3} (\Omega_a + \Omega_b - 2\dot{\phi}) \left[\frac{h}{2} - \left(\frac{1 - \kappa^2}{2 + \kappa^2} \right) \delta \right]. \quad (\text{B } 10)$$

B.2. The squeeze flow, $\mathbf{u}^{\text{S}}(z, \theta)$

The boundary condition are

$$u^{\text{S}}(0, \theta) = w^{\text{S}}(0, \theta) = 0, \quad \text{and} \quad u^{\text{S}}(h, \theta) = \dot{\epsilon} \sin \theta, \quad w^{\text{S}}(h, \theta) = -\dot{\epsilon} \cos \theta, \quad (\text{B } 11)$$

from which it follows that

$$u^{\text{S}}(z, \theta) = \frac{z}{h} \dot{\epsilon} \sin \theta - \frac{p_\theta^{\text{S}}}{2a\rho v} z(h - z) \quad \text{and} \quad p^{\text{S}}(\theta) = \frac{6a^2 \rho v \dot{\epsilon}}{\epsilon h^2}. \quad (\text{B } 12)$$

B.3. Forces and torques

Because the hydrodynamic force is dominated by the lubrication pressure,

$$\mathbf{F}_a = -aL \oint p(\theta) (\hat{\epsilon} \cos \theta + \hat{\chi} \sin \theta) d\theta \equiv f_\epsilon \hat{\epsilon} + f_\chi \hat{\chi}. \quad (\text{B } 13)$$

Owing to the specific symmetries of the induced pressures, we observe that

$$f_\epsilon = -aL \oint p^{\text{S}}(\theta) \cos \theta d\theta, \quad f_\chi = -aL \oint p^{\text{R}}(\theta) \sin \theta d\theta, \quad (\text{B } 14)$$

which can be evaluated to give the formulae (2.5)–(2.6). Symmetry also demands that the torque on the inner cylinder is provided solely by the rotational fluid motion. In particular,

$$T_a \equiv a^2 \rho L v \oint u_z^{\text{R}}(0, \theta) d\theta, \quad (\text{B } 15)$$

which again leads to the formula (2.7).

Appendix C. Adding a rough contact

Frictional contact between the two cylinders demands the inclusion of a contact force, \mathbf{C} , acting on cylinder A , and $-\mathbf{C}$ on cylinder B . The equations of motion become

$$\left. \begin{aligned} m_a \ddot{\mathbf{X}}_a &= \mathbf{F}_a - m_a \mathbf{g} + \mathbf{C}, & m_b \ddot{\mathbf{X}}_b &= \mathbf{F}_b - m_b \mathbf{g} + \mathbf{E} - \mathbf{C}, \\ \frac{1}{2} m_a a^2 \dot{\Omega}_a &= T_a + a C_\chi, & m_b b^2 \dot{\Omega}_b &= T_b + b E_\chi - b C_\chi, \end{aligned} \right\} \quad (\text{C } 1)$$

where $\mathbf{C} = C_\epsilon \hat{\epsilon} + C_\chi$.

Depending on the normal reaction, C_ϵ , the cylinder surfaces become either locked together by the force of friction, C_χ , or slide over one another when that force is less than the imposed traction. Let $\hat{\psi}$ denote the effective angle of friction that characterizes the contact between the two cylinders when they are immersed in oil. Then, the surfaces do not slide over one another when

$$|C_\chi| < |C_\epsilon| \tan \hat{\psi}, \quad \text{implying } b\Omega_b = a\Omega_a.$$

On the other hand, frictional sliding results when we violate this constraint, and then

$$C_\chi = |C_\epsilon| \tan \hat{\psi} \operatorname{sgn}(b\Omega_b - a\Omega_a)$$

(assuming that the coefficients of sliding and static friction are equal).

As before, we make the thin-gap approximation, $\delta \ll a$, in conjunction with lubrication theory for the fluid. A key detail of the latter is that the fluid forces, f_ϵ and f_χ , are order a/δ larger than the torques, T_a and T_b (normal stresses dominate shear stresses in lubrication theory). Consequently, it is evident from (C 1) that the friction force, C_χ , has its main effect in the equation for Ω_a . On the other hand, the normal reaction, C_ϵ , is crucial in balancing the force that pushes the cylinders together. This guides us to take $\tan \hat{\psi} \sim \delta/a$ (implying further that $C_\chi \sim (\delta/a)C_\epsilon$) to supplement the scalings in the reduction scheme of §4.1. Thus, we arrive at the system quoted in §5, where

$$\mathcal{C}_\epsilon = -\frac{C_\epsilon}{am'_a g}, \quad \mathcal{C}_\chi = \frac{\delta C_\chi}{m'_a g}, \quad \tan \psi = \frac{a}{\delta} \tan \hat{\psi}. \quad (\text{C } 2)$$

REFERENCES

- ASHMORE, J., DEL PINO, C. & MULLIN, T. 2005 Cavitation in a lubrication flow between a moving sphere and a boundary. *Phys. Rev. Lett.* **94**, 124501.
- FINN, M. & COX, S. 2001 Stokes flow in a mixer with changing geometry. *J. Engng Maths* **41**, 75–99.
- GOLDMAN, A. J., COX, R. G. & BRENNER, H. 1967 Slow viscous motion of a sphere parallel to a plane wall – I Motion through a quiescent fluid. *Chem. Engng Sci.* **22**, 637–665.
- JEFFREY, D. J. & ONISHI, Y. 1981 The slow motion of a cylinder next to a plane wall. *Q. J. Mech. Appl. Maths* **34**, 129–137.
- PINKUS, O. & STERNLICHT, B. 1961 *Theory of Hydrodynamic Lubrication*. McGraw-Hill.
- PROKUNIN, A. N. 2004 Microcavitation in the slow motion of a solid spherical particle along a wall in a fluid. *Fluid Dyn.* **39**, 771–778.
- SEDDON, J. R. T. & MULLIN, T. 2006 Reverse rotation of a cylinder near a wall. *Phys. Fluids* **18**, 041703.
- SMART, J. R., BEIMFOHR, S. & LEIGHTON, D. T. 1993 Measurement of the translational and rotational velocities of a noncolloidal sphere rolling down a smooth inclined plane at low Reynolds number. *Phys. Fluids A* **5**, 13–24.
- VENER, D. 2006 Rocking and rolling down an incline: the dynamics of nested cylinders on a ramp. PhD Thesis, M.I.T.
- YANG, L., SEDDON, J. R. T., MULLIN, T., DEL PINO, C. & ASHMORE, J. 2006 The motion of a rough particle in a Stokes flow adjacent to a boundary. *J. Fluid Mech.* **557**, 337–346.